



Praseodymium and gadolinium doped ceria as a cathode material for low temperature solid oxide fuel cells



Rajalekshmi Chockalingam^a, Ashok Kumar Ganguli^b, Suddhasatwa Basu^{a,*}

^a Department of Chemical Engineering, Indian Institute of Technology Delhi, New Delhi 110016, India

^b Department of Chemistry, Indian Institute of Technology Delhi, New Delhi 110016, India

H I G H L I G H T S

- $\text{Pr}_x\text{Ce}_{0.95-x}\text{Gd}_{0.05}\text{O}_{2-\delta}$ ($0.15 \leq x \leq 0.4$) is investigated as cathode for LT-SOFC.
- The composition $x = 0.2$ exhibited compatible CTE value with that of GDC.
- The composition $x = 0.2$ demonstrated optimum electronic and ionic conductivity.
- Single cell with PCGO cathode delivered maximum power density 98 mW cm^{-2} at 650°C .

A R T I C L E I N F O

Article history:

Received 10 September 2013

Received in revised form

21 October 2013

Accepted 23 October 2013

Available online 5 November 2013

Keywords:

Solid oxide fuel cell

Cathode material

Ionic transference number

Electronic conductivity

Mixed ionic electronic conductor

A B S T R A C T

Mixed ionic electronic conducting praseodymium and gadolinium doped ceria ($\text{Pr}_x\text{Ce}_{0.95-x}\text{Gd}_{0.05}\text{O}_{2-\delta}$ ($0.15 \leq x \leq 0.40$)) compositions have been studied as a cathode material for low temperature solid oxide fuel cells. Four compositions of $\text{Pr}_x\text{Ce}_{0.95-x}\text{Gd}_{0.05}\text{O}_{2-\delta}$ (PCGO) have been prepared by varying the praseodymium content. Phase formation, thermal expansion, ionic conductivity, electronic conductivity, ionic transference number and electrochemical performance have been investigated. X-ray diffraction results indicate that PCGO samples crystallize in the fluorite structure, and the lattice volume decreases with increasing praseodymium content, x . The coefficient of thermal expansion increases with increasing x , and at $x = 0.2$ shows an optimum value of $12 \times 10^{-6} \text{ K}^{-1}$. Ionic transference number decrease while electronic conductivity increase with increasing x . It has been found that electronic contribution to the total conductivity is higher than ionic contribution for all compositions. The praseodymium doping with cerium dioxide introduces impurity bands within the ceria band gap and facilitates the electronic transition from valance band to conduction band through praseodymium impurity levels. The single cell with configuration, $\text{Pr}_{0.2}\text{Ce}_{0.75-x}\text{Gd}_{0.05}\text{O}_{2-\delta} - \text{Ce}_{0.80}\text{Gd}_{0.20}\text{O}_{2-\delta} \parallel \text{Ce}_{0.80}\text{Gd}_{0.20}\text{O}_{2-\delta} \parallel \text{NiO} - \text{Ce}_{0.80}\text{Gd}_{0.20}\text{O}_{2-\delta}$ delivers a maximum power density of 98 mW cm^{-2} at 650°C .

© 2013 Elsevier B.V. All rights reserved.

1. Introduction

State-of-the-art yttria stabilized zirconia based high temperature solid oxide fuel cells (SOFC) suffer due to higher cost and lower reliability [1]. One of the solutions to the existing problems is to reduce the operating temperature of SOFC [2]. Reducing the operating temperature of SOFC from $800\text{--}1000^\circ\text{C}$ to $500\text{--}700^\circ\text{C}$ would lower the cell degradation rate and fabrication cost through the use of cheaper metallic interconnections and flexible glass sealants [3]. A major issue in reducing the operating temperature of SOFC below 800°C is the poor catalytic activity of existing cathode materials for

electrochemical reduction of oxygen [4]. Hence, the development of new high performance cathode materials, capable of operation at low temperature demands immediate attention. The essential requirements for the low temperature cathode materials are; (i) high mixed ionic and electronic conductivity, (ii) long term stability in oxidizing atmosphere, (iii) thermal and chemical compatibility with that of the electrolyte material and (iv) high catalytic activity for the oxygen reduction reaction at low temperatures [5]. Even though, the conventional cathode material, $\text{La}_{1-x}\text{Sr}_x\text{MnO}_3$ (LSM) satisfies most of the requirements of cathode material at high temperatures for yttria stabilized zirconia (YSZ) electrolyte, its performance at low temperatures ($500\text{--}700^\circ\text{C}$) is poor due to inadequate catalytic activity for oxygen reduction reaction and oxide-ion conductivity [6]. Several groups have investigated perovskites or perovskite-related materials such as $\text{NdBaCo}_{2-x}\text{Cu}_x\text{O}_{5+\delta}$, $\text{GdBaCo}_{1.0}\text{Cu}_{1.0}\text{O}_{5+\delta}$,

* Corresponding author. Tel.: +91 11 26591035; fax: +91 11 26581120.
E-mail address: sbasu@chemical.iitd.ac.in (S. Basu).

$\text{La}_{1-x}\text{Sr}_x\text{Co}_{1-y}\text{Fe}_y\text{O}_{3-\delta}$ (LSCF), $\text{La}_{0.9}\text{Sr}_{0.1}\text{Ga}_{0.8}\text{Mg}_{0.2}\text{O}_{3-\delta}$ (LSGM), $\text{Ba}_{1-x}\text{Sr}_x\text{Co}_{1-y}\text{Fe}_y\text{O}_{3-\delta}$ (BSCF) and $\text{SrCo}_{1-y}\text{Sb}_y\text{O}_{3-\delta}$ (SCS) $\text{DyBaCo}_2\text{O}_{5+\delta}$ as alternative cathode materials for intermediate temperature SOFC applications [3–7]. Despite the large improvements in the area-specific resistance (ASR), these materials do not perform well in the temperature range of 500–700 °C. Another class of materials which is of great interest for the application of intermediate temperature cathode is ceria-based oxides [8]. Pure stoichiometric CeO_2 has fluorite structure in the temperature range of 25–2477 °C and has large tolerance for atomic disorder introduced by doping, oxidation and reduction [9]. When CeO_2 is reduced to CeO_{2-x} , it behaves as a n-type semiconductor at low oxygen partial pressures and p-type semiconductor at high oxygen partial pressures [10]. The addition of divalent or trivalent dopants to these fluorite structures generates oxygen vacancies which are responsible for ionic conduction. Doped ceria has already been extensively studied for a long time as an electrolyte material for intermediate temperature solid oxide fuel cells due to its high ionic conductivity compared to ZrO_2 at intermediate temperatures. Ionic conductivity of ceria is greatly influenced by the type and concentration of the dopant. In recent years, many reports have suggested that praseodymium doped ceria behaves as a mixed ionic and electronic conductor and is appealing as a material for applications as oxygen pumps, oxygen sensors and oxygen separation membranes. Takasu et al. [9] investigated the electrical conductivity of praseodymium doped ceria and found that the composition $\text{Ce}_{0.60}\text{Pr}_{0.40}\text{O}_{2-\delta}$ has high ionic as well as electronic conductivity above 600 °C. Nauer et al. [6] studied praseodymia and niobia doped ceria and observed an increase in electrical conductivity with increasing praseodymium content and reported an ionic conductivity higher than 0.1 S cm^{-1} at 800 °C. They also pointed out that PrO_{2-x} is soluble in CeO_2 up to 30 mol% while addition of 3 mol% of $\text{NbO}_{2-\delta}$ further increased the solubility up to 50 mol%. Stefanik and Tuller [11] investigated the non-stoichiometry and defect chemistry in $\text{Pr}_x\text{Ce}_{1-x}\text{O}_{2-\delta}$ and reported that at low partial pressure of oxygen, a maximum ionic conductivity is exhibited by 10% Pr doped ceria and thereafter conductivity decreased due to defect association. At high partial pressures of oxygen, the conductivity increased above 20% Pr level due to the formation of an impurity band in which electrons and holes are hopping. At Pr level below 20%, Pr^{3+} re-oxidizes to Pr^{4+} , which reduces the oxygen vacancies and decreases the ionic conductivity.

There were also reports of multi doped ceria in order to improve the electrical conductivity by lowering the association enthalpy of oxygen vacancies, increase of configuration entropy, modification of elastic strain in the crystal lattice and change in the grain boundary composition [6]. Maffei and Kuriakose [8] doped ceria with gadolinium and praseodymium to reduce the electronic conductivity of ceria and found that double doping scheme is not effective in reducing the electronic conductivity of ceria. Fagg et al. [12] studied $\text{Zr}_{0.10}\text{Ce}_{0.7}\text{Pr}_{0.2}\text{O}_{2-\delta}$ and observed a variation of average coefficient of thermal expansion (CTE) from 13×10^{-6} to $18 \times 10^{-6} \text{ K}^{-1}$ within the temperature range 30–1000 °C and the material exhibited mixed ionic and electronic conductivity both in reducing and oxidizing conditions. In a recent publication, Fagg et al. [13] further investigated the influence of Gd substitution on thermal expansion behavior of $\text{Ce}_{0.8-x}\text{Pr}_{0.2}\text{O}_{2-\delta}$ and found that 20% Gd addition varied the CTE value from 10×10^{-6} to $18 \times 10^{-6} \text{ K}^{-1}$ within the temperature range of 30–1000 °C. The increase in Gd content, however, decreases the total, ionic and electronic conductivity. Schmale et al. [14] studied the influence of CoO addition on electronic conductivity of $\text{Ce}_{0.8}\text{Gd}_{0.2-x}\text{Pr}_x\text{O}_{2-\delta}$ for the application of oxygen storage materials and oxygen permeability devices. Addition of 2 at% of CoO increases the sinterability and densification of CeO_2 while maintaining high electronic conductivity over a wide range of partial pressures of oxygen, $p\text{O}_2$. The CoO segregates

at the grain boundaries and forms an electronically percolating network of conducting paths which acts as a short circuit and increases the electronic conductivity.

Most of the published work till date on Pr and Gd co-doped CeO_2 have focused its application as an oxygen sensor, or for oxygen storage and oxygen permeability devices and no detailed study has been reported about its suitability as a cathode material for low temperature solid oxide fuel cells. In the present work, attempt has been made to investigate the structural, thermal, optical, electrical and electrochemical properties of the mixed ionic and electronic conducting oxides $\text{Pr}_x\text{Ce}_{0.95-x}\text{Gd}_{0.05}\text{O}_{2-\delta}$ ($0.15 \leq x \leq 0.40$) oxides for the application of low temperature SOFC cathode.

2. Experimental

2.1. Sample preparation, phase, microstructure and optical characterization

Powders of $\text{Pr}_x\text{Ce}_{0.95-x}\text{Gd}_{0.05}\text{O}_{2-\delta}$ (PCGO) with $x = 0.15, 0.20, 0.30$ and 0.40 were prepared by conventional solid state route. High purity oxides of CeO_2 , Gd_2O_3 and Pr_6O_{11} (99.95%, Alfa Aesar, Johnson Matthey Company, USA) in stoichiometric ratio were ball milled in ethanol for 24 h. The resulting powders were dried at 80 °C for 12 h and pre-calcined at 1100 °C for 6 h. The calcined powders were uni-axially die-pressed at 70 MPa into 13 mm diameter pellets. The samples were vacuum-packed and isostatically pressed at 250 MPa for 5 min. The green pellets were sintered at 1600 °C for 10 h in air with a heating and cooling rate of 2 °C per minute.

An X'PERT PRO Panalytical X-ray diffractometer was used to determine the phase and crystal structure of PCGO powder samples. Cu K α radiation was generated with an accelerating voltage of 40 kV and current of 30 mA. Joint Committee on Powder Diffraction Standards (JCPDS) database was used to identify the phases. The average crystallite size (D) was calculated from the reflections of (4 2 2) plane using Scherrer formula, $D = 0.9\lambda/\beta\cos\theta$. Where, λ is the wavelength of X-rays (Cu K α 1.5406 Å), θ is the scattering angle of the main reflections and β is the corrected peak at full width and half maximum (FWHM) intensity [15]. $\beta = \sqrt{\beta_m^2 - \beta_s^2}$ where β_m is the half width of (4 2 2) reflection of $\text{Pr}_x\text{Ce}_{0.95-x}\text{Gd}_{0.05}\text{O}_{2-\delta}$ (PCGO) sample and β_s is the half width of the (4 2 2) reflection in a standard CeO_2 sample. Bulk density of the samples was determined using Archimedes principle using de-ionized water. For this purpose, the test specimens were dried at 110 °C for 20 min and weighed (W_D). The samples were then placed in de-ionized water and boiled for 2 h, subsequently cooled to room temperature and kept for 12 h. Suspended weights (W_S) of the samples were measured with an accuracy of 0.01 g. After determining the suspended weight, the specimens were blotted with a cotton cloth and saturated weights (W_{Sat}) of the samples were measured. The density was calculated using the formula. $\rho = W_D/(W_{\text{Sat}} - W_S)$. Theoretical density of the samples were calculated using XRD technique [16] by using the following equation, $d_{\text{th}} = z \times M/V \times 0.6023$ where M is the mass of one formula unit, z is the number of such chemical unit in 1 unit cell of the crystal, V is the volume of the unit cell as determined by the X-ray diffraction. The microstructures of the sintered samples were evaluated using a scanning electron microscope (SEM). Differential thermal analysis (DTA) and thermogravimetric analysis (TGA) were performed using NETZSCH–TA 45 simultaneous TGA–DTA over a temperature range 25–1000 °C with a heating rate of 5 °C per min in air. The data acquisition and processing were carried out using the software Proteus Analysis. Optical absorption measurements were performed on PCGO samples using Lambda Bio-20, Perkin Elmer UV–Vis spectrometer at room temperature.

2.2. Measurement of coefficient of thermal expansion (CTE) measurement

The thermal expansion measurements were performed in air on the sintered rod shaped specimens with a relative density of >95% using the NETZSCH 402 PC dilatometer over a temperature range 25–800 °C with a heating rate of 2 °C per min. Standard fused silica sample was used for calibration. The samples were cut and polished to cylindrical rods of dimensions of 25.0 mm × 6 mm length and diameter respectively. The average thermal expansion coefficient (α) was calculated from the thermal expansion curve using the formula, $\alpha = 1/L_0(\Delta L/\Delta T)$ where, L_0 is the initial length of the sample; ΔL and ΔT are the change in length and temperature of the test specimen, respectively.

2.3. Electrical conductivity, polarization resistance and transference number measurements

Fig. 1(a) illustrates the cell configuration used to study the conductivity of PCGO cathode compositions ($x = 0.15, 0.20, 0.30$ and 0.40). For this purpose silver paste was brush painted on a fully dense PCGO samples and subsequently dried and fired at 500 °C for 1 h. The conductivity measurements were performed in the temperature range, 550–700 °C in air using a potentiostat–galvanostat (AUTOLAB PGSTAT 30) in the frequency range from 0.1 Hz to 1 MHz with 10 mV signal amplitude. For this purpose samples were heated in a muffle furnace and data were collected at regular intervals with the help of a computer connected to frequency response analyzer (FRA). Before each impedance measurements the cell was equilibrated to the temperature for about 30 min. Air was supplied to the symmetric cells at a continuous flow rate of 30 ml min^{−1} at STP (standard temperature and pressure) inside an alumina tube. Correction files were used to eliminate any resistance due to the leads. All data were collected while sweeping from high to low frequency in order to avoid polarization in the sample. Nyquist plots were then generated using commercially available nonlinear

least square fit software NOVA 1.8 and the conductivity in S cm^{−1} was determined for each composition.

The schematic of a symmetric half-cell used to study the polarization resistance of PCGO cathode is shown in Fig. 1(b). For this purpose, the electrolyte was prepared from commercial gadolinia doped ceria (GDC) (99.99% pure, Sigma Aldrich, USA) powder by preparing a fully dense disk by uni-axial pressing at 30 MPa followed by cold-isostatic pressing at 275 MPa and subsequent sintering at 1600 °C for 5 h in air with a heating and cooling rate of 2 °C per min. The diameter of the sintered GDC electrolyte disk was 10.6 mm and thickness was 1 mm. Porous PCGO electrodes were prepared mixing various compositions of PCGO powders ($x = 0.15, 0.20, 0.30$ and 0.40) with α -terpineol solvent and ethyl cellulose and subsequently ball milled for 24 h. The as prepared ink was brush painted on both sides of a fully dense and polished GDC pellet. The samples were then dried and sintered at 1450 °C for 10 h. For current collection, the electrodes were brush painted with Ag conductive ink and then contacted with Ag wire mesh. The complete symmetrical half-cell assembly with lead wires was mounted on an alumina tube. The alumina tube was then placed into a quartz tube reactor, fitted with gas inlet, outlet. Finally, the quartz reactor was then placed in a split furnace. The AC impedance spectra were recorded as a function of temperature within the frequency range from 1 MHz to 0.1 Hz using a potentiostat–galvanostat (AUTOLAB PGSTAT 30, FRA). The values of the resistance were obtained by using commercially available software NOVA 1.8 with appropriate equivalent circuit model.

The original photograph of a homemade ionic transference number measurement set-up and the schematic are shown in Fig. 2(a) and (b), respectively. For this purpose, a concentration cell with configuration $pO_2', Ag||PCGO||Ag, pO_2''$ was built using two alumina tubes with dimension of 200 mm length and 13 mm inner diameter. The dense PCGO cathode sample was sandwiched between these two tubes using high temperature ceramic cement (AREMCO, Ceramabond, NY) in order to achieve a gas tight sealing. Silver electrodes were brush painted on to the flat surface of the pellet by using silver paste (Alfa Aesar) to assure good electrical contact and silver wires were used as the connection leads. A Pt/Pt–13% Rh thermocouple was used to measure the temperature accurately at the outer surface of the electrode. The gases were supplied to the electrodes through two quartz tubes (outer diameter of 12 mm) compression fitted with the alumina tubes. The whole assembly was kept in a split furnace. Dried and pure oxygen gas was passed on one side (cathode side) as a reference gas and air or mixture of O₂–Ar gases ranging from 5 to 45% O₂ were passed into the anode side of the cell. The flow rate of the gases on both sides of the cell was maintained at a rate of 100 ml min^{−1} using a flow meter. The voltage and current were measured using a potentiostat–galvanostat. The average ionic transference number [17] is calculated using the equation, $t_0 = E_0/E_N$ where E_0 is the reversible thermodynamic potential measured under open circuit conditions across PCGO and E_N is the Nernst potential imposed across the sample. The value of E_N was determined by the activity of electro active species at the electrode–electrolyte interfaces. The E_N is given by Ref. [17]

$$E_N = \frac{RT}{4F} \ln \left[\frac{pO_2''}{pO_2'} \right] \quad (1)$$

where, R is the universal gas constant, T is the absolute temperature, F is the Faraday's constant

pO_2' and pO_2'' are the partial pressures of oxygen at the two interfaces of the cell. Transference number definition assumes that the interfacial processes are infinitely fast. This equation has been used frequently in the literature to calculate the average ionic

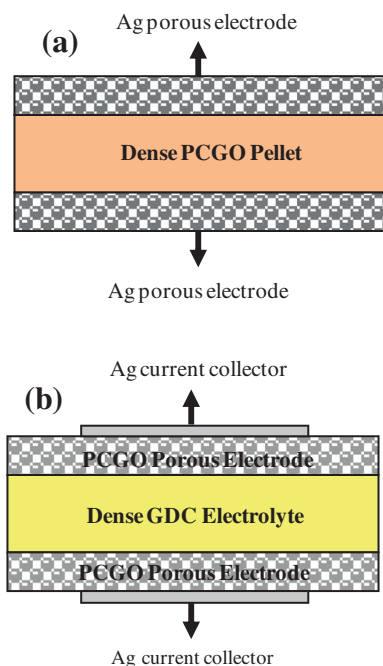


Fig. 1. (a) Schematic of cell configuration used to study the conductivity. (b) Symmetric half-cell configuration used to study the polarization resistance.

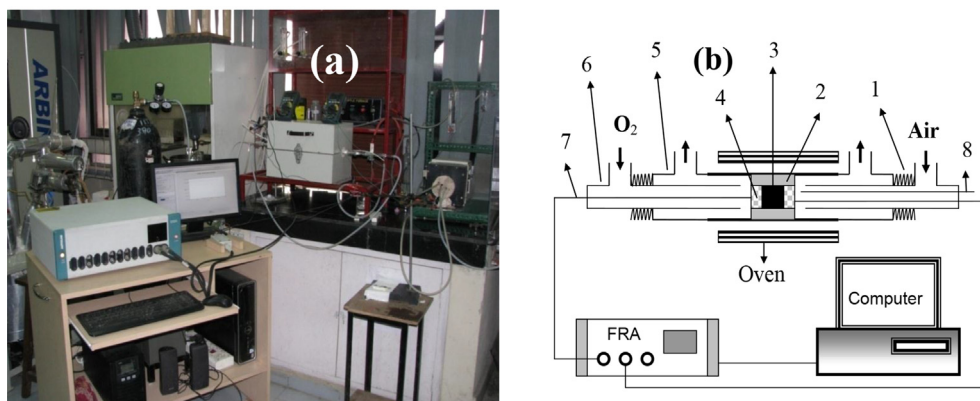


Fig. 2. (a) The photograph of transference number measurement set up, (b) the schematic diagram of transference number measurement set up. (1) Spring, (2) ceramic sealant, (3) sample, (4) silver electros (5) Alumina tube, (6) Gas inlet/outlet (7) silver connecting wires, (8) Pt/Pt–13% Rh thermocouple, quartz tubes.

transference numbers of an MIEC under various conditions [17]. The total conductivity (σ_T) of PCGO samples were obtained by measurement and the ionic conductivity were estimated as; $\sigma_0 = t_0\sigma_T$ and the electronic conductivity has been estimated as $\sigma_e = (1 - t_0)\sigma_T$.

2.4. Electrochemical characterization

In the present study, single cells were fabricated by brush painting the cathode slurry on an anode-electrolyte bilayer prepared by cold-isostatic pressing the respective powders [18]. The anode powder composition was 51 wt% NiO–39 wt% GDC powder and 10 wt% of starch as pore former and GDC powder was used as electrolyte. First, a well-mixed NiO–GDC powder with starch was filled through a mesh into a die of diameter 13 mm followed by GDC electrolyte powder. The anode-electrolyte bilayer was then uniaxially pressed at 70 MPa to form a cylindrical disk shaped pellet and it was iso-statically pressed at 275 MPa of pressure. The isostatically pressed bilayer pellet was brush painted with cathode slurry, comprised of 70:30 wt% PCGO:GDC prepared through solid state reaction route. Ethyl cellulose and poly vinyl butyral were used as binder and plasticizer. The compacted single cells were then sintered at 1550 °C for 10 h in air with controlled heating rate of 2 °C per minute. Anode surface of the sintered cell was covered with nickel gauze and cathode surface was covered with silver gauze as current collectors, which were then coated with silver conductive ink as sealant. Silver wires were used as the connection leads and heat treated at 500 °C, 1 h for a better electrical contact. The single button cell was mounted in between the air and fuel chambers of stainless steel casing and the whole cell set up was connected to the indigenously built fuel cell test station [19]. The cells were tested between 550 and 700 °C with humidified hydrogen gas as the fuel and air as oxidant. Flow rates of gases were controlled between 40 and 100 ml min^{−1} at 1 atm pressure using mass flow controllers. The performance analysis of the fuel cells was carried out using Potentiostat–Galvanostat (Autolab, PGSTAT 30).

3. Results and discussion

3.1. Crystal chemistry

The XRD patterns of $\text{Pr}_x\text{Ce}_{0.95-x}\text{Gd}_{0.05}\text{O}_{2-\delta}$ ($0.15 \leq x \leq 0.40$) samples, sintered at 1550 °C for 5 h are shown in Fig. 3. All the sintered samples show fluorite crystal structure and no extra peaks are observed. The lattice parameters, cell volume and crystallite

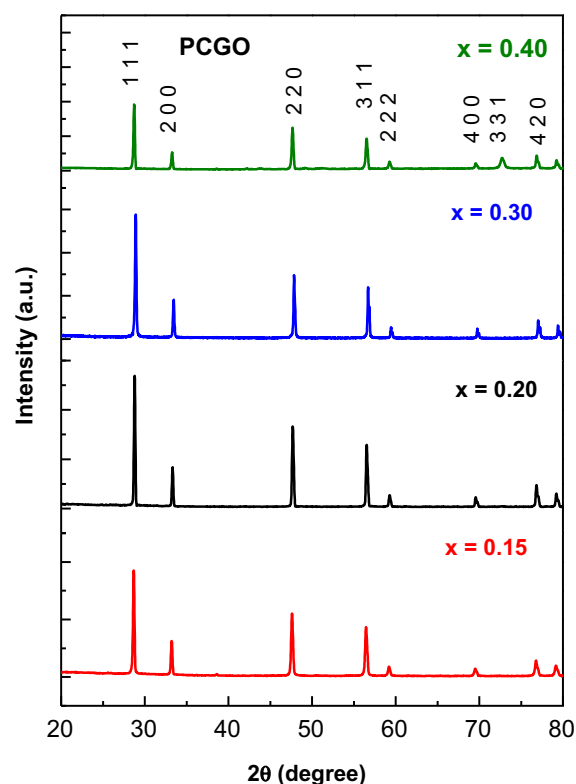


Fig. 3. X-ray diffraction analysis of $\text{Pr}_x\text{Ce}_{0.95-x}\text{Gd}_{0.05}\text{O}_{2-\delta}$ ($0.15 \leq x \leq 0.40$) cathode samples sintered at 1550 °C for 5 h.

size were calculated and listed in Table 1. The values of the lattice parameters of all compositions agree well with that of published

Table 1

Chemical composition, lattice parameters, lattice volume and average crystallite size from Rietveld refinement of the XRD patterns of $\text{Pr}_x\text{Ce}_{0.95-x}\text{Gd}_{0.05}\text{O}_{2-\delta}$ cathode.

Sample ID	Lattice parameter a (Å)	Lattice volume (Å ³)	Density g cm ^{−3}	Crystallite size (nm)
X = 0.00	5.425	159.6	7.30	28.6
X = 0.15	5.422	159.4	7.21	27.5
X = 0.20	5.416	158.9	7.24	31.5
X = 0.30	5.414	158.7	7.25	26.5
X = 0.40	5.409	158.3	7.27	44.9

literature data [9]. The data indicates that the lattice volume decreases with increasing Pr content. This may be due to the formation of oxygen vacancies and replacement of larger radius Ce^{4+} ions (0.97 Å) by smaller radius Pr^{4+} ions (0.95 Å). Takasu et al. [9] and Nauer et al. [6] reported a decrease in lattice parameter with increasing Pr content in CeO_2 . On the contrary, Shuk et al. [15] reported an increase of lattice parameter with increase in Pr content in CeO_2 and argued that the synthesis routes can influence the change in trend of the lattice parameter with Pr content. High temperature synthesis route favors the formation of Pr^{3+} , which has larger ionic radii than Pr^{4+} leading to an increase in lattice parameter with increasing Pr content [15]. Fig. 4 shows the results of TGA analysis of $\text{Pr}_x\text{Ce}_{1-x}\text{Gd}_{0.05}\text{O}_{2-\delta}$ ($0.15 \leq x \leq 0.40$) powder samples performed in air from room temperature to 1000 °C with a heating and cooling rate of 2 °C per minute. The data were also collected while cooling the sample. All the PCGO samples exhibit weight loss above 400 °C. The sample $x = 0.15$ exhibits more weight loss compared to other samples and the weight loss decreases with increasing Pr content. The weight losses are 0.78, 0.40, 0.38 and 0.30 percentages for $x = 0.15, 0.20, 0.30$ and 0.40 , respectively. This weight loss can be attributed to the loss of lattice oxygen described by the following equation [20].



where, $\text{V}_\text{O}^{\times}$ represent oxygen vacancy and $\text{O}_\text{O}^{\times}$ represent oxide ion respectively. The other plausible mechanism may be reduction of smaller Pr^{4+} ion to larger Pr^{3+} ion that is accompanied by loss of oxygen or the transition of Pr^{3+} from the low spin to high spin state [21]. It is generally observed that mixed ionic electronic conducting (MIEC) materials at higher temperatures lose electrons while heating, and gain electrons while cooling [21]. Similar observations have also been previously reported in the $\text{LnBaCo}_{2-x}\text{Cu}_x\text{O}_{5+\delta}$ ($0 < x < 1.0$) [21] and $\text{YBaCo}_{2-x}\text{Cu}_x\text{O}_{5+\delta}$ [22] perovskites systems.

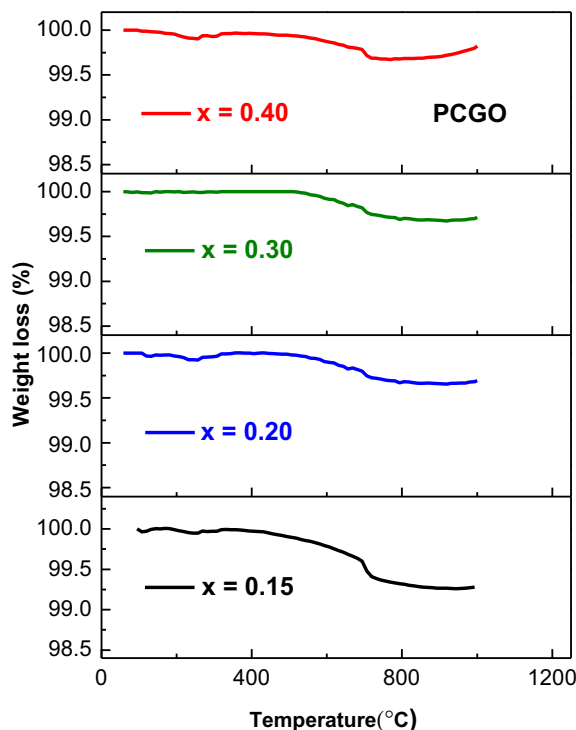


Fig. 4. TGA plots of $\text{Pr}_x\text{Ce}_{0.95-x}\text{Gd}_{0.05}\text{O}_{2-\delta}$ ($0.15 \leq x \leq 0.40$) recorded in air with a heating rate of 2 °C min⁻¹.

The results indicate that the ionic compensation mechanism is dominating for the sample $x = 0.15$, whereas electronic compensation mechanism is dominating for $x = 0.40$. In other words, the ionic compensation mechanism decreases and electronic compensation mechanism increases with increasing Pr content.

3.2. Thermal expansion behavior

The linear thermal expansion plots for $\text{Pr}_x\text{Ce}_{0.95-x}\text{Gd}_{0.05}\text{O}_{2-\delta}$ ($x = 0.15, 0.20, 0.30, 0.40$) is shown Fig. 5. All the four compositions exhibit identical behavior up to 500 °C and thereafter the slope increases with increasing Pr content. The increase in slope of the curves at high temperatures may be due to the loss of lattice oxygen [23]. The formation of V_O in combination with thermal reduction of Pr^{4+} and Ce^{4+} cations to lower valence Pr^{3+} and Ce^{3+} causes increase in the unit cell volume due to larger size of the Pr^{3+} (1.11 Å) and Ce^{3+} (1.13 Å) ions compared to Pr^{4+} (0.95 Å) and Ce^{4+} (0.97 Å) ions. Further, the previous work by Logan and Shelef [24] showed that Pr addition in ceria shifts the reduction to lower temperatures. Thermal reduction temperature of Pr^{4+} to Pr^{3+} in CeO_2 is 875 °C and Pr^{4+} to Pr^{3+} in Pr_6O_{11} is 575 °C respectively. It is interesting to note that the addition of 20% Pr into CeO_2 ($\text{Ce}_{0.77}\text{Pr}_{0.23}\text{O}_x$) shifted the reduction temperature of Ce^{4+} to Ce^{3+} at 550 °C. One can also clearly see that the slope of the curve which represent the compositions $x = 0.30$ and $x = 0.40$ is steeper than that of $x = 0.15$ and $x = 0.20$. This may be due to the increase in thermal expansion caused by higher concentration of Pr^{4+} ions, Ce^{4+} ions and oxygen vacancies present in the sample.

Coefficient of thermal expansion is another important parameter that influences the performance of SOFC. Large variations in the CTE values of the electrodes and electrolytes cause thermal stress, leading to crack formation during thermal cycling [25,26]. Coefficient of thermal expansion of PCGO calculated from the thermal expansion curves by linear regression in the temperature range 25–800 °C as a function of Pr content is shown in the inset of Fig. 5. The PCGO sample, $x = 0.15$ exhibits CTE value of $15.7 \times 10^{-6} \text{ K}^{-1}$ and $x = 0.20$ exhibits a CTE value of $13 \times 10^{-6} \text{ K}^{-1}$, which is close to the value of GDC electrolyte $12.6 \times 10^{-6} \text{ K}^{-1}$. On the other hand, the CTE values of the compositions $x = 0.30$ and $x = 0.40$ exhibit higher CTE values of 18.4×10^{-6} and $19.6 \times 10^{-6} \text{ K}^{-1}$, respectively. The larger increase in the thermal

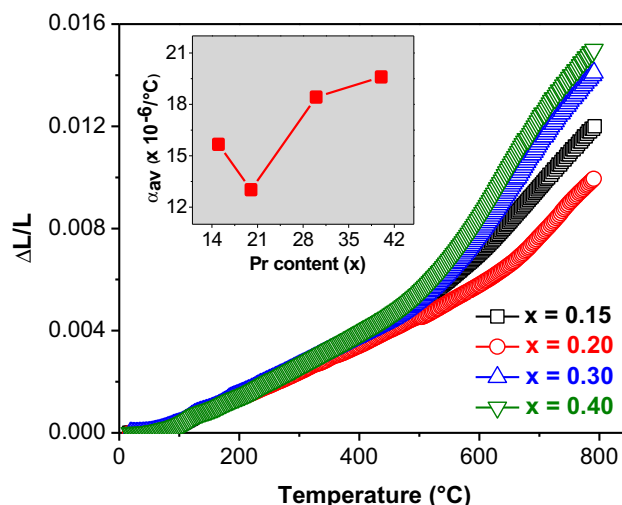


Fig. 5. Linear thermal expansion curves of $\text{Pr}_x\text{Ce}_{0.95-x}\text{Gd}_{0.05}\text{O}_{2-\delta}$ ($0.15 \leq x \leq 0.40$) (PCGO) as a function of temperature measured in air. Inset shows the coefficient of thermal expansion (CTE) of PCGO as a function of Pr content measured from 25 to 800 °C.

expansion coefficient of the compositions $x = 0.30$ and $x = 0.40$ is due to the loss of oxygen and associated reduction of Pr^{4+} to Pr^{3+} and Ce^{4+} to Ce^{3+} . The occurrence of a minimum in thermal expansion for the composition $x = 0.20$ has not been clarified and needs further investigation. The results indicate that the PCGO with 0.20% Pr could be a potential candidate material as cathode for low temperature solid oxide fuel cells with GDC as electrolyte.

3.3. Impedance spectroscopy analysis

AC impedance measurements were carried out in the temperature range of 550–700 °C with symmetric half-cell configuration [27], PCGO//GDC//PCGO in air. AC impedance plots of $\text{Pr}_x\text{Ce}_{0.95-x}\text{Gd}_{0.05}\text{O}_{2-\delta}$ ($0.15 \leq x \leq 0.40$) as a function of Pr content measured at various temperatures are presented in Fig. 6. The typical impedance spectra show two semi depressed arcs one at high frequency and another at low frequency. The shape of impedance curve is not completely developed at low temperature (550 °C) as expected because of low conductivity. The shape of the arc is similar to that reported in the literature for LSCF//GDC//LSCF symmetric cell [28]. Nauer et al. [6] investigated praseodymia and niobia doped ceria to evaluate the possibility of using these materials as cathodes for solid oxide fuel cells. They observed two semi circles in the impedance spectra, when the ionic contribution to the total conductivity is appreciable and one semicircle appears when the electronic conductivity is much higher than the ionic one. Similar observations have been reported in the case of lanthanum–barium–cobalt oxide and gadolinium doped ceria composite cathode, [29–32]. The high frequency arc signifies charge transfer process including oxygen ion diffusion through the bulk and charge transfer at the electrode/electrolyte interface. The low frequency arc signifies non-charge transfer process including oxygen surface

exchange and oxygen gas diffusion [29]. It is evident from Fig. 6 that high frequency resistance decreases with increasing temperature as well as Pr content for all the compositions. The low frequency resistance decreased with increasing Pr content at 550 °C and no trend has been observed above 550 °C. Similarly, the composition $x = 0.20$ and 0.40 show decrease in resistance with increase in temperature and no trend has been observed in $x = 0.15$. This may be due to variations in microstructural parameters such as triple phase boundary length, pore size and contact area between electrode–electrolyte interfaces from one sample to another. Moreover, the amplitudes of the high frequency arcs were found to be lower than that of the low frequency arcs due to decrease in time constant [30]. The data obtained from impedance curves were evaluated by fitting an equivalent circuit model using the commercially available software, NOVA 1.8. The work on de-convoluting different phenomena associated with impedance curves are going on and perhaps be communicated separately.

The Arrhenius plot of the low frequency resistance is shown in Fig. 7(a). It can clearly be observed that the resistance of low frequency process decreases slowly with an increasing temperature. The $x = 0.20$ composition exhibits the highest resistance throughout the temperature range, whereas $x = 0.40$ exhibits lowest resistance throughout the temperature range. The activation energies associated with low frequency resistance varies from 0.07 eV ($x = 0.20$) to 0.12 eV ($x = 0.40$). The lower activation energy indicates that enhanced oxygen diffusion takes place due to the optimal porosity and good contact between cathode and the electrolyte. The Arrhenius plot of the high frequency resistance is shown in Fig. 7(b). The $x = 0.15$ composition shows high resistance and $x = 0.40$ shows low resistance throughout the temperature range. The activation energies associated with high frequency resistance are 0.27 eV ($x = 0.40$) and 0.56 eV ($x = 0.20$), which is

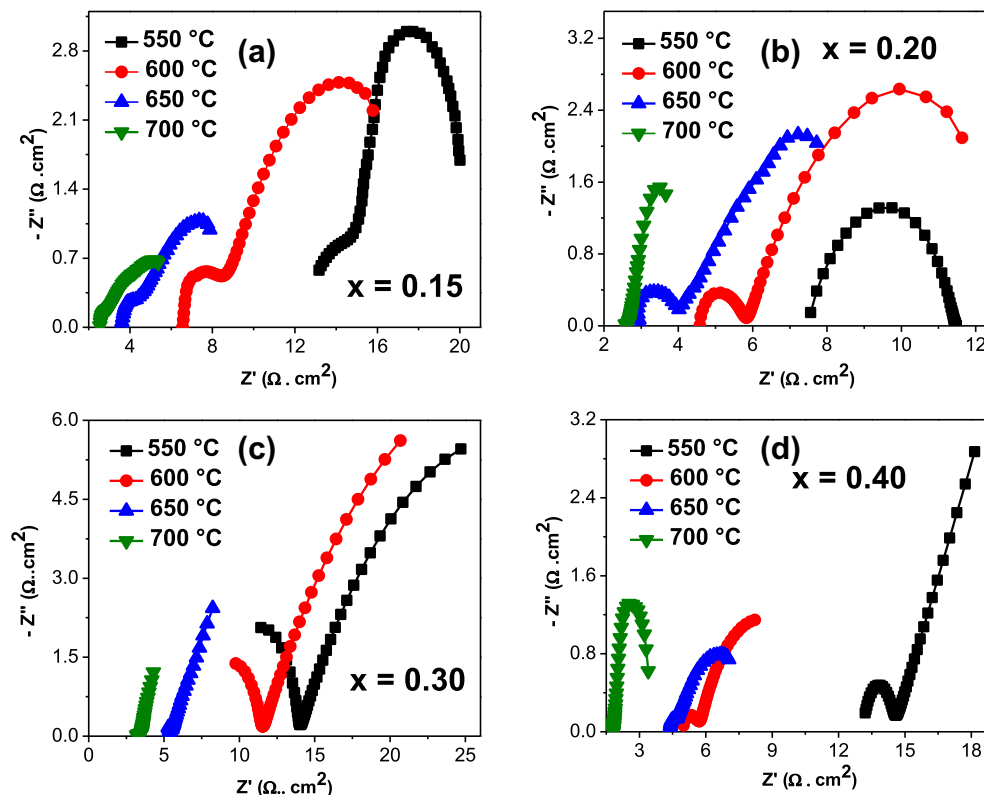


Fig. 6. AC impedance plots of PCGO compositions (a) $\text{Pr}_{0.15}\text{Ce}_{0.80}\text{Gd}_{0.05}\text{O}_{2-\delta}$ (b) $\text{Pr}_{0.20}\text{Ce}_{0.75}\text{Gd}_{0.05}\text{O}_{2-\delta}$ (c) $\text{Pr}_{0.30}\text{Ce}_{0.65}\text{Gd}_{0.05}\text{O}_{2-\delta}$ (d) $\text{Pr}_{0.40}\text{Ce}_{0.55}\text{Gd}_{0.05}\text{O}_{2-\delta}$ measured at temperatures ranging from 550 to 700 °C.

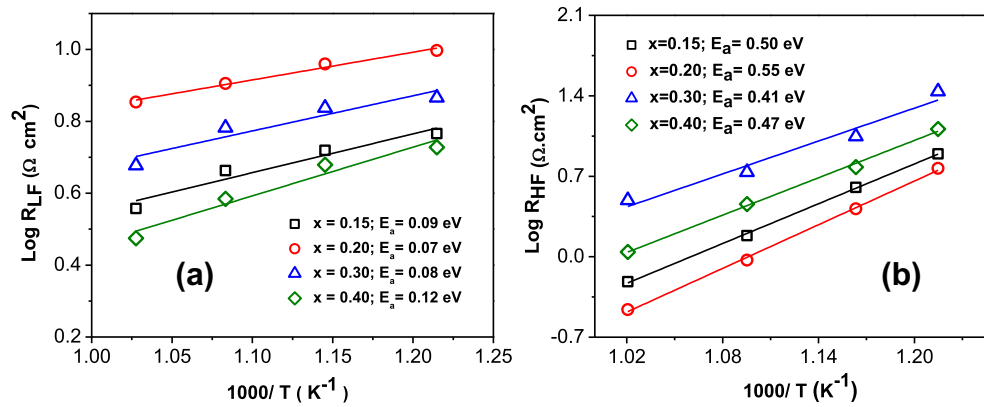


Fig. 7. (a) Temperature dependence of the polarization resistance and activation energy obtained by fitting the low frequency and (b) high frequency impedance plots to the equivalent electrical circuit.

lower than those of the reported values of low temperature cathode material. Amin et al. [30] reported activation energy associated with high frequency resistance is around 1.2 eV for lanthanum–barium–cobalt oxide–gadolinium-doped-cerium oxide (LBC–GDC) composite cathode. Kim and Manthiram [21] reported 1.25, 1.02 and 1.11 eV for $\text{LaSr}_3\text{Fe}_{1.5}\text{Co}_{1.5}\text{O}_{10}$ (LSFC) + GDC; $\text{NdSr}_3\text{Fe}_{1.5}\text{Co}_{1.5}\text{O}_{10}$ (NSFC) + GDC; $\text{NdSr}_{2.5}\text{Ca}_{0.5}\text{Fe}_{1.5}\text{Co}_{1.5}\text{O}_{10}$ (NSFCFC) + GDC, respectively. It is also interesting to note that the $x = 0.20$ composition shows a single slope for both low frequency as well as high frequency Arrhenius plots indicating that the controlling mechanism for oxygen reduction reaction remains unchanged in the temperature range investigated in this work (400–700 °C). On the other hand, other compositions show multiple slopes indicating more than one controlling mechanism for oxygen reduction reaction. Trejo et al. [33] pointed out that for the fluorite phase material, the activation energy of 0.4 eV, indicates polaronic conduction. This statement can be extended to PCGO, since Schmale et al. [14]

reported an enhanced electronic conduction in PCGO due to reduction in the band width caused by the formation of an impurity band in between the O-2p valence band and the Ce-4f conduction band. Based on the above facts, one can argue that enhanced electronic conductivity is responsible for the improved conductivity at lower temperature.

3.4. Ionic transference number, total, ionic and electronic conductivity

The total conductivity of PCGO samples measured as a function of temperature is seen in Fig. 8(a). The conductivity increases with increasing Pr content above 650 °C. It is interesting to note that the composition, $x = 0.20$ exhibits higher conductivity up to 600 °C compared to other compositions. Table 2 shows the activation energy calculated from the slope of the plot of $\log(\sigma T)$ versus $1/T$. The lowest activation energy of 0.47 eV is exhibited by $x = 0.40$ and

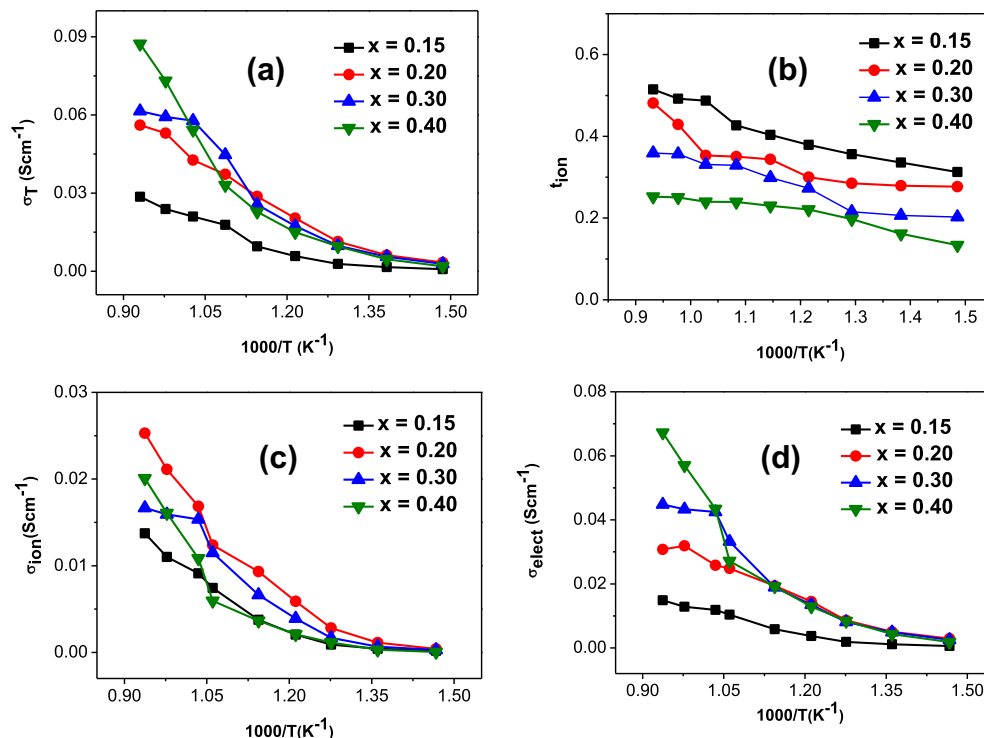


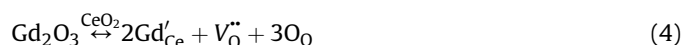
Fig. 8. Total conductivity, transference number, ionic conductivity and electronic conductivity of PCGO compositions as a function of temperature.

Table 2

The Activation energy calculated from Arrhenius Equation of various of $\text{Pr}_x\text{Ce}_{0.95-x}\text{Gd}_{0.05}\text{O}_{2-\delta}$ cathode materials at different temperatures.

Sr. no.	Sample	Temp. (°C)	Slope	E_a (eV)	R^2
1	$X = 0.15$	350–800	6.013	0.53	0.953
2	$X = 0.20$	350–800	7.105	0.61	0.977
3	$X = 0.30$	350–800	6.477	0.56	0.926
4	$X = 0.40$	350–800	5.482	0.47	0.989

highest activation energy of 0.61 is exhibited by $x = 0.2$. Fig. 8(b) shows the ionic transference number of sintered PCGO compositions with $x = 0.15, 0.20, 0.30$ and 0.40 as a function of temperature. From the figure it is evident that the ionic transference number (t_0) decreases with decreasing temperature and increasing Pr content. The results of ionic conductivity as a function of temperature are presented in Fig. 8(c). The ionic conductivity increased with increasing temperature for all the compositions. In the case of $\text{Pr}_x\text{Ce}_{0.95-x}\text{Gd}_{0.05}\text{O}_{2-\delta}$ both Gd and Pr contribute oxygen vacancies as described by the following defect equations [34].



At high oxygen partial pressures and temperatures $[\text{Pr}'_{\text{Ce}}] \gg [\text{Ce}'_{\text{Ce}}]$ and $[\text{Gd}'_{\text{Ce}}] \gg [\text{Ce}'_{\text{Ce}}]$ the electro neutrality condition is

$$[\text{Pr}'_{\text{Ce}}] + [\text{Gd}'_{\text{Ce}}] = 2[\text{V}_\text{O}^{\bullet\bullet}] \quad (5)$$

The composition, $x = 0.20$ exhibited enhanced ionic conductivity compared to other compositions throughout the temperature range. Possible reason for this decreased conductivity for $x = 0.30$ and $x = 0.40$ at high temperature is due to the ordering of oxygen vacancies as observed in the case of fluorite oxide materials [35,36]. As the values of x increases, vacancies become energetically favorable for the formation of vacancy associates and clusters, thereby reduces the ionic conductivity. The results of electronic conductivity as a function of temperature are presented in Fig. 8(d). The compositions $x = 0.20, 0.30$ and 0.40 showed similar trend from 400 to 600 °C, thereafter the electronic conductivity increased with increasing Pr content and temperature. Recently, Kim et al. [37] reported significant electronic conductivity in praseodymium doped ceria (PCO) due to optically induced electronic transitions from valence band to conduction band through an impurity band formed within the CeO_2 band gap by Pr. This unusual feature in PCO is also observed in $\text{SrTi}_{1-x}\text{Fe}_x\text{O}_{3-\delta}$ [38]. The optical absorption measurements in UV–visible range are performed covering from 300 to 800 nm on all four PCGO compositions ($x = 0.15, 0.20, 0.30$ and 0.40) and 20 mol% GDC. The results are presented in Fig. 9. It is clearly evident from the figure that the absorption spectra shift to higher wavelength side when the amount of Pr in GDC is increased. The calculated band gap of pure GDC is 3.03 eV, which is close to the reported value (3.5 eV) in the literature [39]. The band gap is reduced from 3.03 to 1.88 eV, when GDC is doped with 15 mol% Pr. The band gap is further reduced to 1.61 eV, when the amount of Pr is increased to 40 mol%. It is observed that yellow colored GDC powder changed to reddish tint color when GDC is doped with Pr. The color change is due to the excitation of electrons from valance band to empty Pr^{4+} electronic states which aids the optical absorption in the visible range [39]. In the present study, the increase in electronic conductivity with increasing Pr content is correlated to band gap reduction. Pr doping introduces impurity bands within the ceria band gap and facilitates the electronic transition from O-2p valance band to Ce-4f conduction band through Pr impurity band [37].

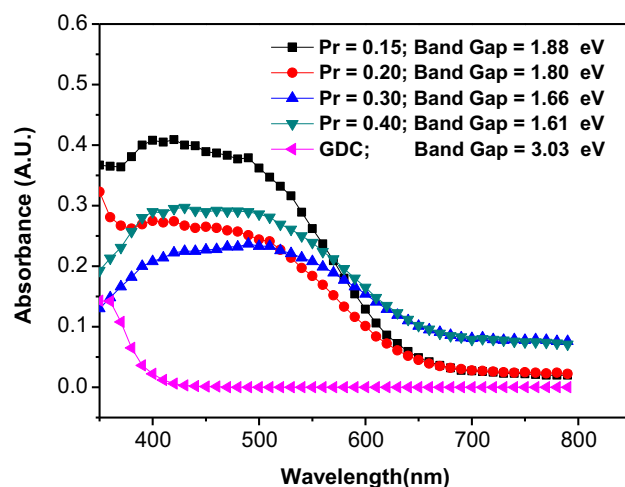


Fig. 9. Optical absorption spectra of $\text{Pr}_x\text{Ce}_{0.95-x}\text{Gd}_{0.05}\text{O}_{2-\delta}$ ($0.15 \leq x \leq 0.40$) measured in UV–visible range covering from 300 to 800 nm.

3.5. Current voltage characteristics

Single cells with configuration $\text{NiO-GDC} \parallel \text{GDC} \parallel \text{Pr}_{0.2}\text{Ce}_{0.75}\text{Gd}_{0.05}\text{O}_{2-\delta} \text{—GDC}$ was fabricated as an anode supported cell. Fig. 10 illustrates SEM micrograph of the cross section of sintered single cell, which clearly shows porous anode, cathode and dense electrolyte. The thickness of both cathode and electrolyte layers were $\sim 450 \mu\text{m}$ and the anode layer was $\sim 550 \mu\text{m}$. The performance analysis of single cell was conducted at a temperature ranging from 550 to 700 °C. Humidified H_2 was used as the fuel and air was used as the oxidant. The comparison of open circuit voltage, current density and power density for three different temperatures are presented in Fig. 11. It is evident from the figure that the current density and power density increased with increase in temperature. The single cell delivered a maximum power density of 74, 98 and 160 mW cm^{-2} at 550, 650 and 700 °C respectively. The corresponding ASR values estimated from AC impedance spectra were 0.24, 0.23 and $0.17 \Omega \text{ cm}^2$. Fig. 12 shows XRD phase analysis results of the chemical stability test performed on $\text{Pr}_{0.2}\text{Ce}_{0.75}\text{Gd}_{0.05}\text{O}_{2-\delta}$ —GDC composite powder heat treated at room temperature, 650 °C for 50 h, and 1050 °C for 50 h

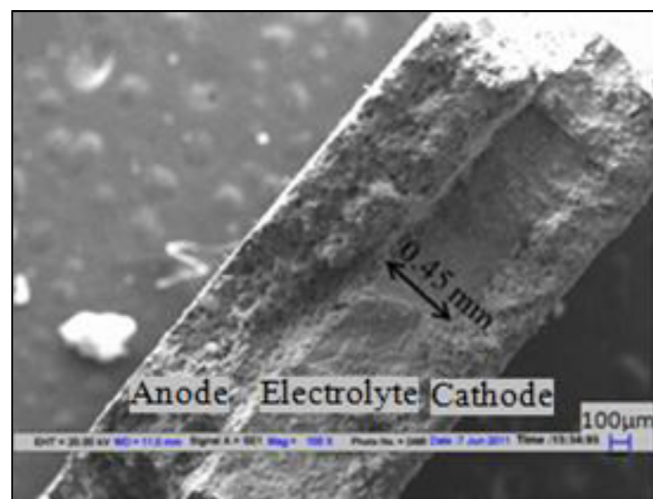


Fig. 10. SEM microstructure showing cross section NiO-GDC anode, GDC electrolyte and PCGO-GDC cathode of the fracture surface of a $\text{NiO-GDC} \parallel \text{GDC} \parallel \text{Pr}_{0.2}\text{Ce}_{0.75}\text{Gd}_{0.05}\text{O}_{2-\delta} \text{—GDC}$ single cell after the cell test.

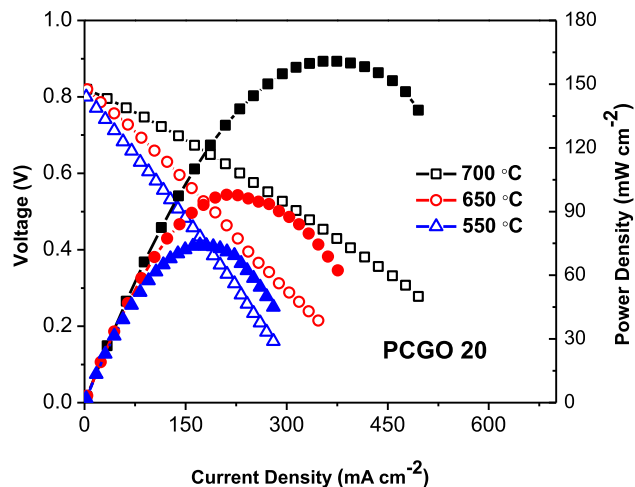


Fig. 11. Performance analysis of NiO-GDC||GDC||Pr_{0.2}Ce_{0.75}Gd_{0.05}O_{2-δ}-GDC single cell measured at 500, 600 and 700 °C.

respectively. No additional phase formation has been detected in the X-ray analysis indicating that PCGO is not reacting with GDC and retained the fluorite structure.

4. Conclusions

The cathode composition, Pr_{0.20}Ce_{0.75}Gd_{0.05}O_{2-δ} exhibits high-est ionic conductivity, electronic conductivity at 550 °C. It also shows a CTE value of $13 \times 10^{-6} \text{ K}^{-1}$ in the temperature range of 25–800 °C. The ionic transference number of Pr_xCe_{0.95-x}Gd_{0.05}O_{2-δ} decreases with increasing Pr content indicates that the electronic contribution to total conductivity increases with increasing Pr

content due to the formation of an impurity band in between O-2p valence band and the Ce-4f conduction band, which in turn reduces the band gap. Both Gd and Pr contribute to the improvement in ionic conductivity. The better electrochemical performances of Pr_xCe_{0.95-x}Gd_{0.05}O_{2-δ} with increasing Pr content are correlated to enhanced ionic and electronic conduction. Single cells having configurations NiO-GDC||GDC||Pr_{0.2}Ce_{0.75}Gd_{0.05}O_{2-δ}-GDC delivered a maximum power density of 74, 98 and 160 mW cm⁻² at 550, 650 and 700 °C respectively. Preliminary results show that electronic conductivity as well as cathode microstructure needs to be further improved to use as a practical cathode material for low temperature SOFC applications.

Acknowledgments

Authors are gratefully acknowledged the financial support of this research by Council of Scientific and Industrial Research (CSIR), New Delhi, India Project No: 22(0524)/10/EMR-II and I.I.T. Delhi.

Symbols

α	average thermal expansion coefficient (K ⁻¹)
β	corrected peak at full width half maximum
D	crystallite size (nm)
ΔL	change in length of the specimen (mm)
ΔT	change in temperature (°C)
d_{th}	theoretical density (g cm ⁻³)
E_0	reversible thermodynamic potential (V)
E_N	Nernst potential (V)
F	Faraday's constant ($9.65 \times 10^4 \text{ C mol}^{-1}$)
λ	wavelength (nm)
L_0	initial length of the sample (mm)
p_{O_2}	partial pressure of oxygen (atm)
R	universal gas constant ($8.314 \text{ J mol}^{-1} \text{ K}^{-1}$)
ρ	bulk density (g cm ⁻³)
σ	conductivity (S cm ⁻¹)
σ_T	total conductivity (S cm ⁻¹)
σ_e	electronic conductivity (S cm ⁻¹)
σ_0	ionic conductivity (S cm ⁻¹)
T	absolute temperature (K)
t_0	ionic transference number (–)
V_O^-	vacancy of oxygen
W_D	dry weight (g)
W_{Sat}	saturated weight (g)
W_S	suspended weigh

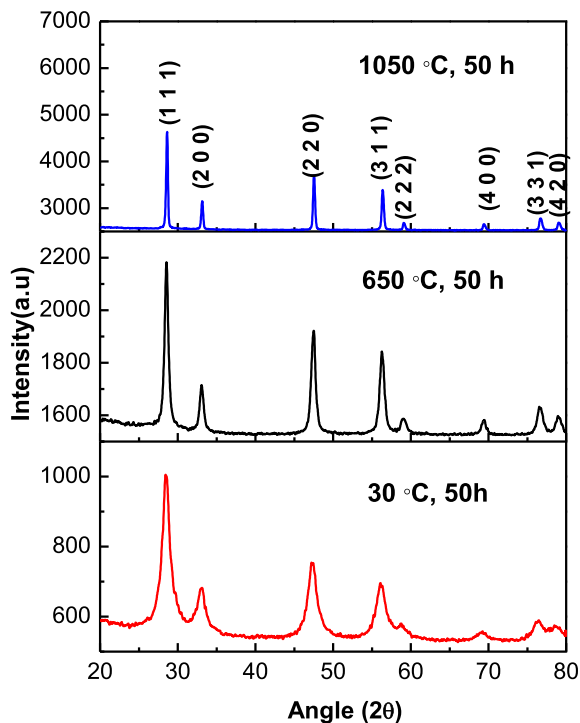


Fig. 12. Chemical stability of Pr_{0.20}Ce_{0.75}Gd_{0.05}O_{2-δ} cathode against GDC electrolyte. The data were collected after heating a (1:1) mixture of the PCGO cathode and GDC electrolyte powders 650, 1050 °C for 50 h in air; followed by recording the XRD patterns at room temperature.

References

- [1] M.L. Perry, T.F. Fuller, J. Electrochem. Soc. 149 (2002) S59–S67.
- [2] J.W. Fergus, J. Power Sources 162 (2006) 30–40.
- [3] B.C.H. Steele, Solid State Ionics 134 (2000) 3–20.
- [4] P. Bance, N.P. Brandon, B. Girvan, P. Holbeche, S. O'Dea, B.C.H. Steele, J. Power Sources 131 (2004) 86–90.
- [5] Z. Shao, S.M. Haile, Nature 431 (2004) 170–173.
- [6] M. Nauer, C. Ftikos, B.C.H. Steele, J. Eur. Ceram. Soc. 14 (1994) 493–499.
- [7] M.W. Xiong, X. Yuan, J.W. Yin, Y.M. Yin, Z.F. Ma, Ceram. Int. 39 (2013) 4481–4488.
- [8] N. Maffei, A.K. Kuriakose, Solid State Ionics 107 (1997) 67–71.
- [9] Y. Takasu, T. Sugino, Y. Matsuda, J. Appl. Electrochem. 14 (1984) 79–81.
- [10] W. Huang, P. Shuk, M. Greenblatt, Solid State Ionics 113–115 (1998) 305–310.
- [11] T.S. Stefanik, H.L. Tuller, J. Electroceram. 13 (2004) 799–803.
- [12] D.P. Fagg, J.R. Frade, V.V. Kharton, I.P. Marozau, J. Solid State Chem. 179 (2006) 1469–1477.
- [13] D.P. Fagg, I.P. Marozau, A.L. Shaula, V.V. Kharton, J.R. Frade, J. Solid State Chem. 179 (2006) 3347–3356.
- [14] K. Schmale, M. Grunebaum, M. Janssen, S. Baumann, F.S. Kupperts, H.D. Wiemhofer, Phys. Status Solidi B 248 (2011) 314–322.
- [15] P. Shuk, M. Greenblatt, Solid State Ionics 116 (1999) 217–223.

- [16] W.D. Callister, *Materials Science and Engineering: an Introduction*, John Wiley & Sons, New York, 2007, p. 37.
- [17] V.V. Kharton, F.M.B. Marques, *Solid State Ionics* 140 (2001) 381–394.
- [18] C. Xia, M. Liu, *Solid State Ionics* 144 (2001) 249–255.
- [19] R. Chockalingam, S. Basu, *Int. J. Hydrogen Energy* 36 (2011) 14977–14983.
- [20] X. Ding, X. Kong, J. Jiang, C. Cui, X. Guo, *Mater. Res. Bull.* 45 (2010) 1271–1277.
- [21] Y.N. Kim, A. Manthiram, *J. Electrochem. Soc.* 158 (2011) B41206–B41210.
- [22] X. Zhang, H. Hao, X. Hu, *Phys. B* 403 (2008) 3406–3409.
- [23] J. Lu, Y.M. Yin, Z.F. Ma, *Int. J. Hydrogen Energy* 38 (2013) 10527–105333.
- [24] A.D. Logan, M. Shelef, *J. Mater. Res.* 19 (1994) 468–475.
- [25] G. Xiao, Q. Liu, F. Zhao, L. Zhang, C. Xia, F. Chen, *J. Electrochem. Soc.* 158 (2011) B455–B460.
- [26] M. Godickemeier, K. Sasaki, L.J. Gauckler, *J. Electrochem. Soc.* 144 (1997) 1635–1646.
- [27] D. Han, H. Wu, J. Li, S. Wang, Z. Zhan, *J. Power Sources* 246 (2014) 409–416.
- [28] C.S. Hsu, B.H. Wang, *J. Electrochem. Soc.* 153 (2006) A1478–A1483.
- [29] N. Imanishi, T. Matsumura, Y. Sumiya, K. Yoshimura, A. Hirano, Y. Takeda, D. Mori, R. Kanno, *Solid State Ionics* 174 (2004) 245–252.
- [30] R. Amin, B. Kenney, K. Karan, *J. Electrochem. Soc.* 158 (2011) B1076–B1082.
- [31] C. Lalanne, F. Mauvy, E. Siebert, M.L. Fontaine, J.M. Bassat, F. Ansart, P. Stevens, J.C. Grenier, *J. Eur. Ceram. Soc.* 27 (2007) 4195–4198.
- [32] S. Kim, J. Maier, *J. Electrochem. Soc.* 149 (2002) J73–J83.
- [33] E.R. Trejo, G. Tavizon, H.G. Ortega, *J. Electrochem. Soc.* 154 (2007) A70–A74.
- [34] M. Mogensen, N.M. Sammes, G.A. Tompsett, *Solid State Ionics* 129 (2000) 63–94.
- [35] L. Navarro, F. Marques, J. Frade, *J. Electrochem. Soc.* 144 (1997) 267–273.
- [36] R. Chockalingam, S. Chockalingam, V.R.W. Amarakoon, *J. Power Sources* 196 (2011) 1808–1817.
- [37] J.J. Kim, S.R. Bishop, N. Thompson, Y. Kuru, H.L. Tuller, *Solid State Ionics* 225 (2012) 198–200.
- [38] H.L. Tuller, S.R. Bishop, D. Chen, Y. Kuru, J.J. Kim, T.S. Stefanik, *Solid State Ionics* 225 (2012) 194–197.
- [39] W. Jung, H.L. Tuller, *Solid State Ionics* 180 (2009) 843–847.